HOKKAIDO UNIVERSITY

Title	Accuracy verification of protoacoustic measurements in a heterogeneous phantom by an optical hydrophone
Author(s)	Chen, Ye; Kasamatsu, Koki; Kuriyama, Yasutoshi et al.
Citation	Medical physics, 52(3), 1893-1902 https://doi.org/10.1002/mp.17575
Issue Date	2025-03
Doc URL	https://hdl.handle.net/2115/97369
Rights	This is the peer reviewed version of the following article: Chen Y, Kasamatsu K, Kuriyama Y, et al. Accuracy verification of protoacoustic measurements in a heterogeneous phantom by an optical hydrophone. Med Phys. 2025; 52: 1893-1902, which has been published in final form at https://doi.org/10.1002/mp.17575. This article may be used for non-commercial purposes in accordance with Wiley Terms and Conditions for Use of Self-Archived Versions. This article may not be enhanced, enriched or otherwise transformed into a derivative work, without express permission from Wiley or by statutory rights under applicable legislation. Copyright notices must not be removed, obscured or modified. The article must be linked to Wiley's version of record on Wiley Online Library and any embedding, framing or otherwise making available the article or pages thereof by third parties from platforms, services and websites other than Wiley Online Library must be prohibited.
Type	journal article
File Information	Manuscript_MedPhys_Matsuura_rev20241119_clean.pdf

Hokkaido University Collection of Scholarly and Academic Papers : HUSCAP

Accuracy verification of protoacoustic measurements in a heterogeneous phantom by an optical hydrophone

Running title: Optical hydrophone for protoacoustics

Ye Chen[1], Koki Kasamatsu[2], Yasutoshi Kuriyama[3], Tomonori Uesugi[3], Yoshihiro Ishi[3], Taichi Murakami[1], Sena Hidani[1], Michael Caulfield[1,4], Mehmet Burcin Unlu[5], Wolfgang Rohringer[6], Taeko Matsuura[1*]

[1]Faculty of Engineering, Hokkaido University, Sapporo, Japan

[2]Institute for Quantum Medical Science, National Institutes for Quantum Science and Technology (QST), Chiba, Japan

[3]Institute for Integrated Radiation and Nuclear Science, Kyoto University, Osaka, Japan

[4]Faculty of Engineering, University of Alberta, Edmonton, Canada

[5]Faculty of Engineering, Ozyegin University, Cekmekoy, Istanbul, Turkey

[6]XARION Laser Acoustics GmbH, Vienna, Austria

Keywords: proton therapy, protoacoustics, optical hydrophone

***Corresponding author**:

Dr. Taeko Matsuura, Faculty of Engineering, Hokkaido University, North-15 West-7, Kita-ku, Sapporo, Hokkaido, 060-8638, Japan. Tel: +81-11-706-5254;

Email: taeko.matsuura@eng.hokudai.ac.jp

Abstract

Background: Protoacoustics has emerged as a promising real-time range measurement method for proton therapy. Optical hydrophones (OHs) are considered suitable to detect protoacoustic waves owing to their ultracompact size and high sensitivity. In our previous research, we demonstrated that the time-of-arrival (TOA) measured by an OH showed good agreement with the simulated ground truth in a homogeneous medium.

Purpose: The purpose of the study was to experimentally evaluate the accuracy of the TOA and compression peak pressures detected by the OH. Protoacoustic waves that undergo the typical distortions occurring in the human body were investigated. In such cases, the use of small detectors such as OHs is desirable to minimize the effects of detector size and directivity.

Methods: A 100-MeV proton pencil beam emitted from a fixed-field alternating gradient accelerator was irradiated onto a homogeneous water phantom and a water phantom with a half- or full-sized silicone plate downstream of the Bragg peak (BP) or a bone plate that covered half of the beam cross-section in the beam path. The OH was shifted 70 mm laterally across the beam axis downstream of the BP to measure the protoacoustic waves. The k-WAVE acoustic wave transport simulation was employed as the ground truth. The TOA and the first compression peak pressures were compared between the simulation and experiment.

Results: The TOA deviation against the ground truth was primarily attributed to alignment errors of the measurement devices and phantoms, with deviations of <1 mm. The peak pressure distribution closely resembled the ground truth, with FWHM differences of 0.0%–3.0% for the tested geometries.

Conclusions: The OH was able to determine the TOA and peak pressures with sufficient accuracy in heterogeneous phantoms, even without considering the effect of the size of the detector or directivity on the measurements.

1. Introduction

Protoacoustics, or ionoacoustics, has emerged as a promising method for in-vivo range detection and dose reconstruction in proton therapy[1,2,3]. A deposited dose is converted to the pressure source immediately after delivery of a short-pulsed proton beam, and the generated thermoacoustic wave is detected at the patient surface. Unlike positron emitter tomography or prompt γ-detection methods, which have been clinically used in some institutions[4,5,6], protoacoustics is still in the research phase and has not been clinically used, except for the pioneering research conducted by Hayakawa et al[7]. However, this technique benefits from the compact detector and high compatibility with ultrahigh dose rate radiation (FLASH)[8,9,10] and image-guided radiotherapy (IGRT)[11].

The time-of-arrival (TOA) technique is the simplest among the available protoacoustic range detection techniques, utilizing the time interval between the beam irradiation timing and the arrival of ultrasound waves at the detector. This technique of focusing on the clinically relevant beam energies was initially investigated by Tada *et al.*[12] and Jones *et al.*[13] in homogeneous geometries, namely water phantom and whale muscle. Jones *et al.*[13] demonstrated the measurement of TOA based on compression peaks to be a robust method, which provides the most consistent measure of the distance to the Bragg peak (BP). Although the achievable range accuracy according to these studies was limited to a few millimeters, Lehrack *et al.*[14] demonstrated that employing a clinical synchrocyclotron with a short pulse (<10 μs) could enable achieving submillimeter localization accuracy of the BP. Subsequently, Patch *et al.*[15] and Schauer *et al.*[16] measured the TOA in abdominal phantoms and successfully localized the position of the BP. In these studies, most measurements were conducted close to the beam axis behind the BP, where the TOA is not subject to substantial variation with the scale of the detector size. As such, it can be reasonably assumed that the results were not considerably influenced by the size of the detector. However, at an off-axis region or if the wave is deformed by tissue heterogeneities, the phase of the incident wave can vary over the detector area, thereby potentially influencing the measurement of TOA [13,17]. In addition to range measurement using TOA, beam profile measurement by scanning the transducer in two dimensions using protoacoustic pressure has been successfully demonstrated in previous research [17,18]. Also in such measurements, the detector size is expected to affect the accuracy of beam size estimation.

To minimize the impact of the detector size, miniature detectors such as optical hydrophones (OHs) have an advantage because miniaturization does not sacrifice the sensitivity, unlike the conventional piezo-based detectors used in the aforementioned studies [19,20]. Our previous study has demonstrated that the TOA measured using an OH closely matched the simulated ground truth in a homogeneous medium[11]. However, whether the TOA can be accurately detected in heterogeneous phantoms and/or at off-axis regions, where the spatial variation of the waveforms is non-negligible, remains unclear. Furthermore, it is necessary to ascertain whether the angular sensitivity of OHs affects pressure measurements, despite being expected to be minimal[19]. In fact, the wavefront of a protoacoustic wave does not always coincide with the detector surface, particularly for off-axis measurements or in the presence of heterogeneities.

This study aimed to evaluate the accuracy of an OH in measuring the TOA and pressure magnitude, for protoacoustic waves that undergo typical distortions occurring in the human body. Four heterogeneous geometries with known acoustic properties and relative stopping powers were tested and compared with the protoacoustic simulations previously employed in numerous studies. The measurements were conducted downstream of the BP, which is practically the most important sensor position because the sensitivity of the TOA to the beam range is maximum and the pressure magnitude is high. In addition to the on-axis positions, off-axis positions were tested to investigate the maximum distance from the beam axis at which the accuracy is maintained and whether the directivity of the incident wave affects the measurement accuracy.

2. Methods

2.1 Experiment

A 100-MeV proton pencil beam emitted from a fixed-field alternating gradient accelerator (FFA) [21,22] was irradiated onto a water phantom (Figure 1). FFA characteristics were as previously described[11,23] with a pulse width of approximately 30 ns while pulses were transported at 30 Hz. The number of particles per pulse in this study was $4.0-5.7 \times 10^7$, corresponding to the BP dose of 0.24−0.34 Gy in homogeneous water. A scintillator installed at the

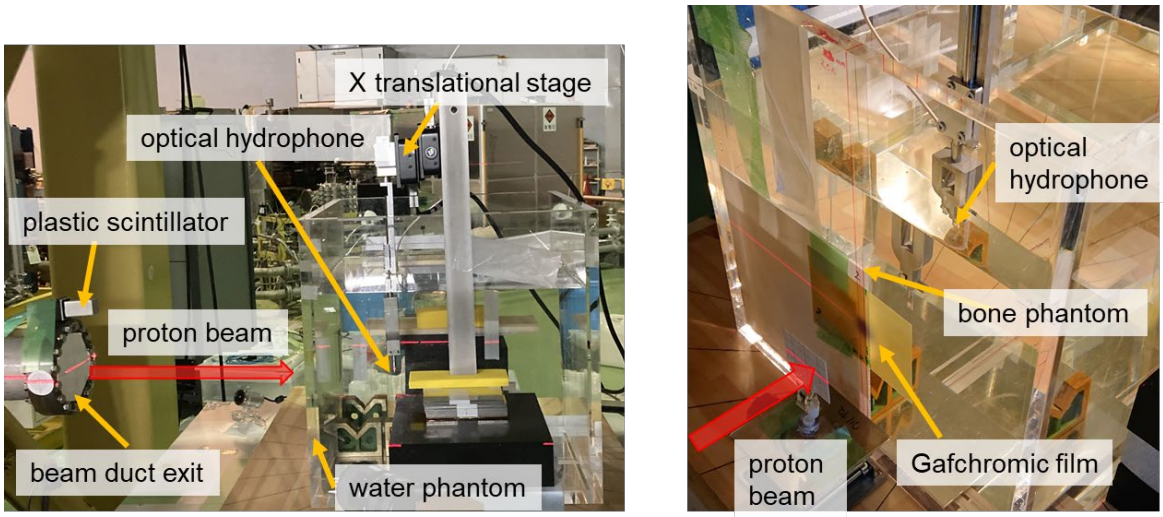


Figure 1. Illustration of the experimental geometry (left) and beam alignment verification by the film (right).

beam exit monitored the pulse width and particle counts. The correlation between the scintillator pulse height and the Faraday cup particle counts was measured offline, and the scintillator pulse height was converted to the number of protons during the experiment.

As shown in Figure 2, the tested geometry consists of (A) a homogeneous water phantom, (B) a water phantom with a 10 mm-thick silicone plate downstream of the beam that is sufficiently wider than the beam size, (C) a water phantom with a 10 mm-thick silicone plate downstream of the beam that covers only half of the beam cross-section, and (D) a water phantom with a 20-mm thick bone plate (Kyoto Kagaku Ltd. Japan) covering only half of the beam cross-section on the beam axis. (B) was considered as a representative geometry with longitudinal heterogeneity for ultrasound waves,[17] and (C) with lateral heterogeneity. (D) is a representative example of a geometry with lateral heterogeneity for proton beams. The water phantom was enclosed by a 15-mm thick acrylic wall. The proton beam range (defined here as the dose maximum of the BP) in (A)−(D) was 56.5 mm from the acrylic inner wall, whereas in (D) the BP splits into two with respective ranges of 43.8 and 56.5 mm. The phantom and beam alignment were performed as follows: First, the beamline was marked by lasers. Then, the lateral position of the proton beam was adjusted using several fluorescent screens placed along the beamline. Then, the water phantom and the bone/silicone plates were aligned using the laser markers. Before each measurement, the Gafchromic film (Ashland Inc. US)

attached to the entrance surface of the water phantom was used to confirm that the beam center coincided with the edge line of the bone/silicone plates (Figure 1).

The relative stopping powers of the acrylic walls, silicone, and bone plates were measured using Gafchromic films and are summarized in Table 1; the sound speed and density are also shown in Table 1. The sound speeds of the silicone and bone plates were measured by the pulsed-echo method, while values for acrylic were taken from the datasheet[24]. The Grüneisen coefficients for converting the transferred energy into the source pressure were taken from previous studies for the acrylic and water[25] and the bone plate[15]. Grüneisen coefficients were not assigned to silicone because this was placed outside the beam path.

The optical hydrophone Eta250L (XARION Laser Acoustics GmbH, Austria) was used for protoacoustic detection[11,19]. The hydrophone uses Fabry–Perot interference, and the detection area is limited to a laser line element size (2×0.35 mm^2). As shown in Figure 2, the laser line of the hydrophone (0.35-mm width) is set vertically to the X-axis. The hydrophone was set using the laser marker and moved with an X-stage over the range of -35 mm $\leq X \leq 35$ mm across the beam axis at a 100-mm depth from the acrylic inner wall. This measurement range was considered sufficient for verification since the sound pressure generally decreases with movement away from the beam axis, making it difficult to observe. In (A) and (B), where the geometry was symmetric, the positive half of the X-axis ($0 \leq X \leq 35$ mm) was measured at a 1-mm pitch, and the negative half of the X-axis was measured at multiple points at a 5-mm pitch to compensate for the X-axis shift of the detector. In (C) and (D), the whole range was measured at a 1-mm pitch. During the measurement, 1000 samples were recorded. In pre-processing, each sample was passed through a 40 dB amplifier and a 150 kHz low-pass filter and recorded on the digital oscilloscope. In post-processing, the data was averaged and then further filtered by the 150 kHz low-pass filter to suppress the noise. We also obtained the data directly on the oscilloscope, followed by post-processing. The delay introduced by the pre-processing was determined by the time difference between the compression peaks of these two signals, which was found to be 2.4 μs. Finally, the RF kicker noise generated at the beginning of the beam delivery was obtained from the background measurement and subtracted from the signal.

Table 1. Properties of materials used in the simulation.

	Water	Silicone plate	Bone plate	Acrylic
Sound speed (m/s)	1490 (22.6℃)	997	2400	2930
Density (g/cm^3)	1.0	1.2	1.8	1.2
Relative stopping power	1	-	1.64	1.16
Grüneisen constant	0.11	-	3.28	1.29

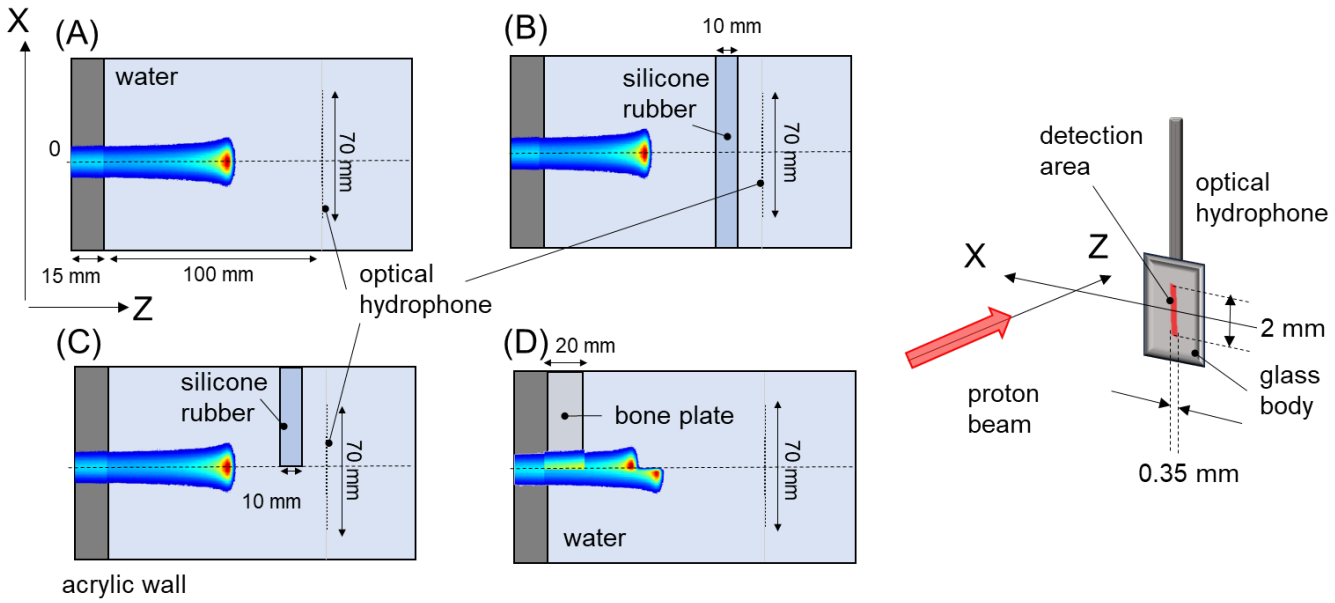


Figure 2. Schematics of phantom geometries: (A) homogeneous water phantom, (B) full-sized silicone plate downstream of the BP, (C) half-sized silicone plate downstream of the BP, and (D) half-sized bone plate in the beam path. Before entering the water, the proton beam passes through the 15-mm thick acrylic wall. The OH is shifted from X = −35 mm to +35 mm through 1-mm increments in the experiment. The right figure illustrates the sensor setup geometry, where the laser direction is aligned vertically to the X-axis.

2.2 Simulations

Simulations, treated as a ground truth in this study, were performed using the Geant4 Monte Carlo simulation (ver. 10.6.p02) for energy transfer calculations[26] and k-WAVE for protoacoustic wave transport calculations[27]. To adjust the Monte Carlo simulation parameters (beam energy, beam size, and angular spread), the beam range, defined as the maximum dose depth in the study, and the lateral beam profiles were obtained using Gafchromic film just before the

protoacoustic measurement at four positions of 16, 25, 40, and 55 cm from the exit of the beam duct. The beam range was 73.9 mm in water-equivalent thickness. The beam energy fluctuation was assumed to be 0.75%, following the BP chamber measurement by Takayanagi et al[28]. The characteristics of each phantom used in the Geant4 and k-WAVE simulations are summarized in Table 1. The composition of the bone plate was taken from the manufacturer's data sheet (Table S1 in Supplementary Material), and the density was set to 1.76 g/cm^3 to reproduce the measured relative stopping power. The simulation was run with 10^7 protons, and the voxel size and grid size were set to 0.33 mm and $300 \times 300 \times 300$, respectively. G4EmStandardPhysics option 3 was used to model the electromagnetism and the binary cascade model was selected for the nuclear interaction.

k-WAVE simulates the following wave equation;

$$\frac{1}{v^2}\frac{\partial^2 p}{\partial t^2} - \nabla^2 p = (\Gamma/v^2)E(\vec{r})I'(t),$$

where Γ and v denote the Grüneisen coefficient and sound speed of the medium, respectively. $E(\vec{r})$ [J/m^3] is the energy density transferred by protons, and $I'(t)$ denotes the time derivative of the normalized beam current [1/s], with the time integral of $I(t)$ over $-\infty < t < \infty$ normalized to 1. Since the FFA has an impulse-like time structure, $I(t)$ was approximated by a delta function. The voxel size and time step were set to 0.33 mm and 10 ns, respectively, giving a Courant–Friedrichs–Lewy number of 0.04 and a maximum supported frequency of 2.2 MHz. The calculation grid size was set to $300 \times 300 \times 400$. In this simulation, the absorption of the sound pressure was not considered, and the sensor was assumed to be a point with constant frequency sensitivity.

2.3 Analysis

The bipolar-shaped γ-waves generated by the BP arrive at the detector either as they are ((A) and (D)) or distorted by acoustic inhomogeneities ((B) and (C)). Here, the TOA of the first compression peak (t_{peak}) and the peak sound pressure (P_{peak}) were compared between simulation and experiment. In system (D), the TOA of the second compression peak and its pressure magnitudes were also compared because BP develops simultaneously at two locations.

Two types of measurement errors are associated with t_{peak}. The first is the alignment error of the detector, stage, and phantom against the proton beam. The translational error in the X-direction for the detector and stage installation was corrected using the symmetry of the reference system (A). However, the measurement of geometry (D) was performed on a different day, so no correction was made. Before each measurement, the beam alignment was verified at the incident plane on the water phantom using a film measurement of the beam profile (Figure 1).

Furthermore, there may be an alignment error of approximately 1 mm in the Z-direction of the detector and stage because they were installed using laser markers. In addition, the translational error in the X-direction remains in geometry (D), and the tilt of the water phantom may be present for all geometries. To convert these alignment errors in the XZ-plane (mm) to the error in t_{peak} (μs), we defined a distance–time conversion coefficient $S\ [\mu s/mm]$ as the maximum slope of t_{peak} in the XZ-plane, i.e., $S = |\nabla t_{peak}| = \sqrt{\left(\partial_X t_{peak}\right)^2 + \left(\partial_Z t_{peak}\right)^2}$ and calculated this coefficient by the simulation. We assumed that a total alignment error of 1 mm is possible under all measurement conditions, and defined the corresponding TOA error as $\sigma_t^A = S\,\Delta x$ where $\Delta x = 1$[mm].

The other error factor is a random error, which is a variation of t_{peak} that is mainly due to electromagnetic noise. Herein, we considered the standard error of the mean, defined as σ_t^R. To estimate this quantity, we first divided the 1000 measurements into N_g = 20 groups of 50 measurements each and then averaged the waveforms within each group to identify the peak. σ_t^R was obtained by dividing the standard deviation of the N_g samples of t_{peak} by $\sqrt{N_g}$.[16]

For the sound pressure, P_{peak} was plotted against the detection axis (X-axis) for each geometry (A)–(D), and the FWHM of the simulation and experiment were compared. The pressure-voltage conversion coefficients provided by the manufacturer are known to have uncertainty and may not give the correct absolute pressure for the protoacoustic waves[11,29]. Therefore, as an alternative, for geometries (A)–(C) acquired on the same day, the conversion coefficient was determined by the ratio of the simulated and experimental data at the center position (X = 0) of (A) and applied to all measurement points in (A)–(C). For (D), since data were obtained on a different day, the conversion coefficient was redetermined at X = 0 and applied to all measurement points.

3. Results

3.1 Comparison of protoacoustic waveforms between experiment and measurement

Figure 3 demonstrates comparisons of the representative waveforms for the tested geometries between the experiment and simulation. In the Supplementary Material, the simulated protoacoustic wave propagations in the XZ-plane have been demonstrated in Movie S1-S4. Note that the waveforms that arrive after 65 μs from the beam irradiation are the resonances from the acrylic walls and bone plate. As shown in Figure 3, as for the first compression peaks, nearly identical TOA and peak width were achieved in the experiment and simulation. Despite this, because of the echoes generated in the detector's internal structures, a major discrepancy was observed following the first peak. In particular, in geometry (D), the echo was large enough to shift the TOA and magnify the peak pressure of the second peak.

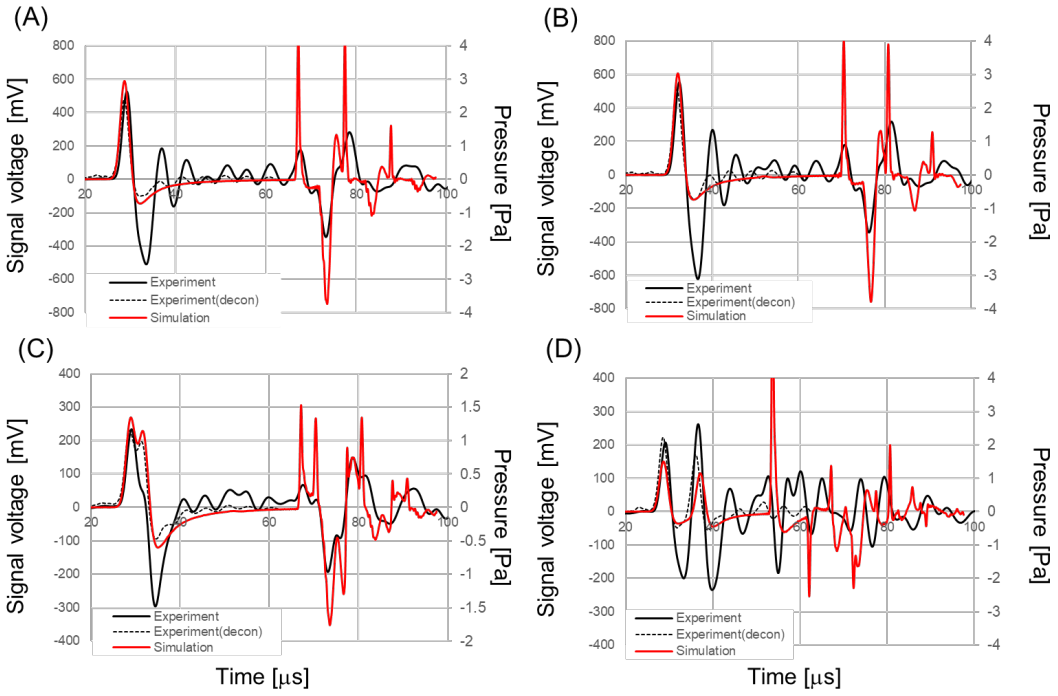


Figure 3. Typical waveforms detected by the OH (black) compared with the simulation (red). (A)–(D) indicates the geometries depicted in Figure 2, and in each figure, the waveform obtained at X = 0 was plotted. The experimental data and the deconvoluted data (dashed black curve explained in the Discussion) are plotted with respect to the left axis while the simulated data is plotted with respect to the right axis. The pressure is demonstrated for 10^8 protons.

3.2 TOA

(A) *Homogeneous water phantom*

The comparison of TOAs of the γ-waves in geometry (A) between simulation and experiment is shown in Figure 4 (a-1). By using the symmetry of the data obtained at X = ±20 mm, X was shifted by 1 mm. The TOA differences were within 1 μs at all positions (Figure 4 (a-1)), and when converted to distance by S, they were <1 mm (Figure 4 (b-1)). Figure 5 shows a comparison of σ_t^R and σ_t^A for all measurement points. As can be seen in the figure, σ_t^R increases as the sensor moves away from the beam axis, reflecting the decrease in sound pressure. Nevertheless, σ_t^R is sufficiently small compared with σ_t^A at all positions. Thus, hereafter, only σ_t^A is shown as error bars in the TOA plots.

The signal-to-noise ratio is sufficiently high in the current experiment due to the combined use of OH and FFA. If the magnitude of the noise is defined as the root mean square of the noise and the signal size is defined as the compression peak voltage of 1000-fold averaged data, then the aforementioned ratio at X=0 was found to be 13.7, 16.1, and 6.9 for geometries (A) through (C), and 5.2 and 6.4 for the first and second compression peaks of geometry (D), respectively.

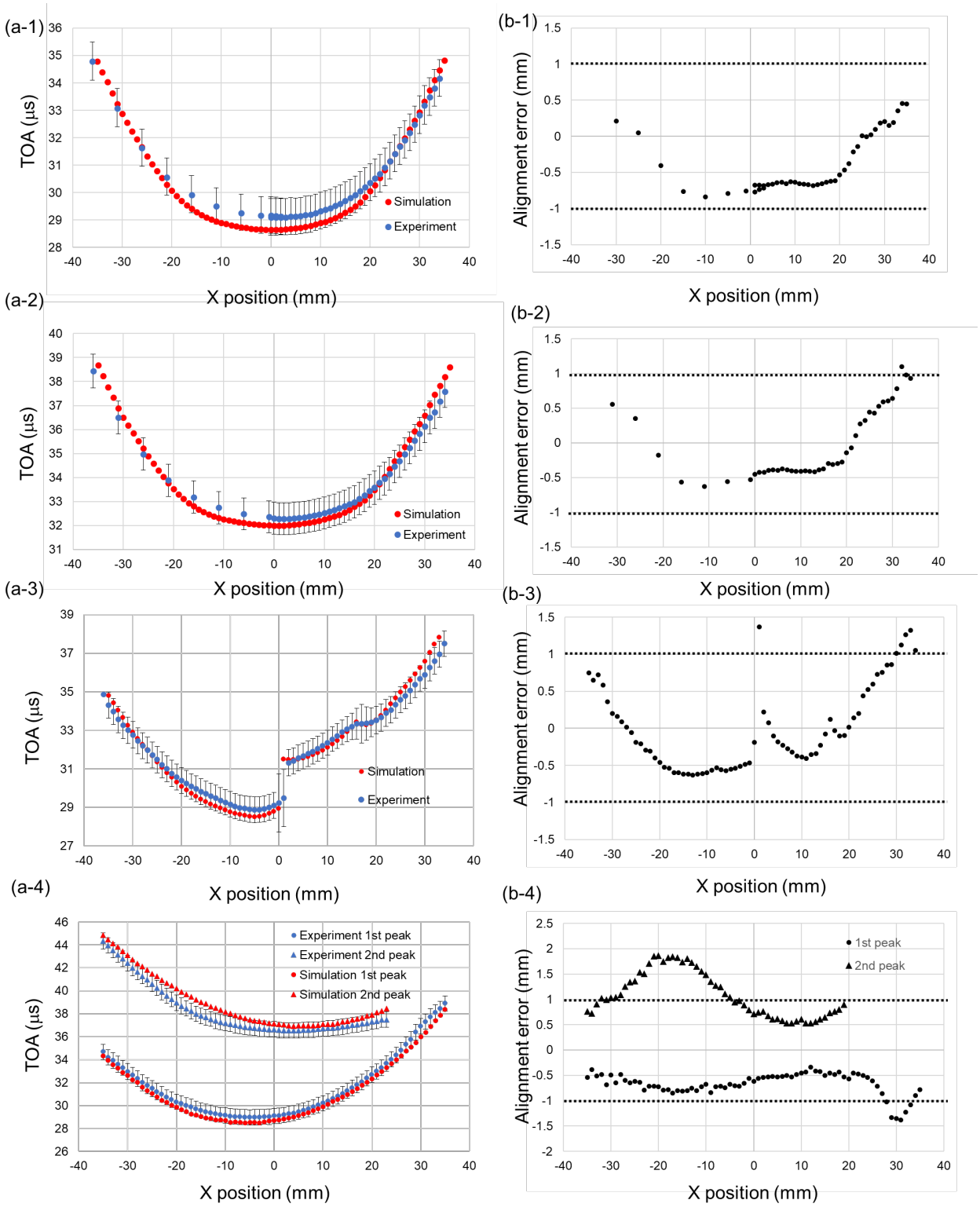


Figure 4. (a) TOA comparison between simulation (red circle) and experiment (blue circle); (b) TOA difference converted to alignment errors by the conversion coefficient. Error bars in (a) show the TOA shift corresponding to 1 mm of alignment error. (a-1) and (b-1) are for geometry (A), (a-2) and (b-2) for geometry (B), (a-3) and (b-3) for geometry (C), and (a-4) and (b-4) for geometry (D).

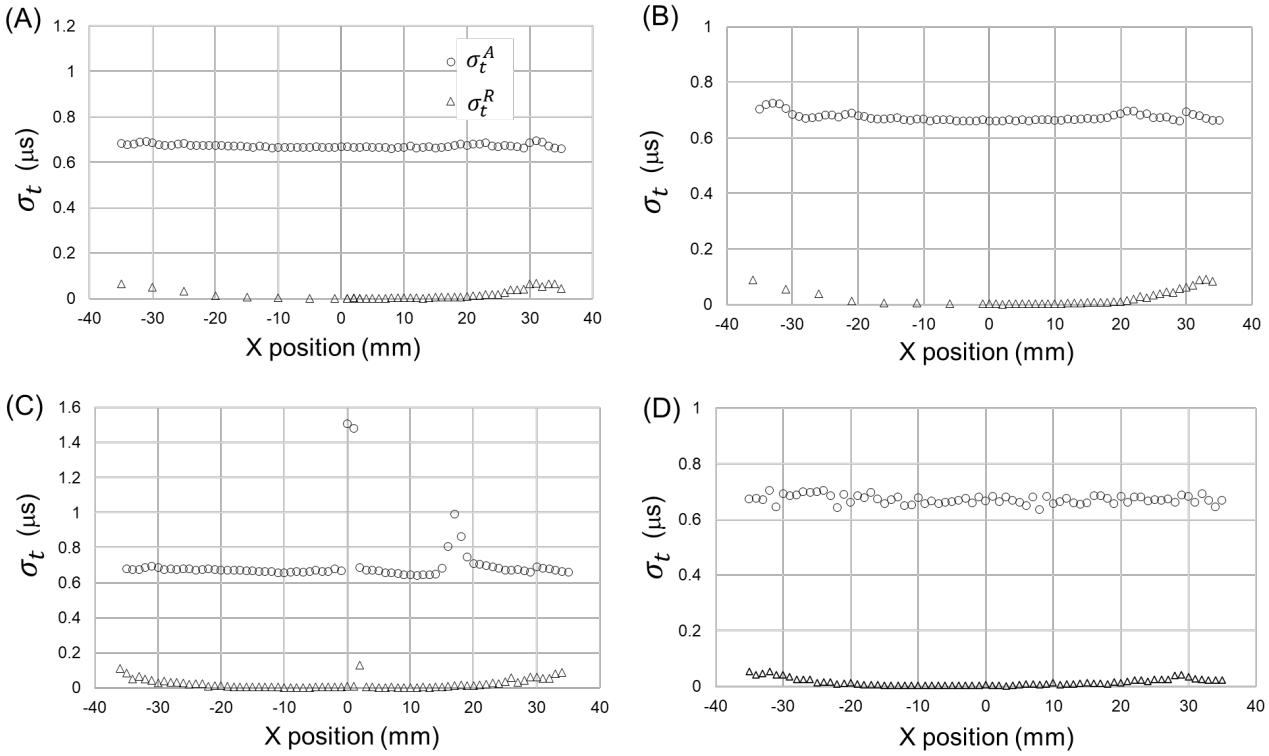


Figure 5. Comparison of σ_t^A (circle) and σ_t^R (triangle) for geometry (A)−(D).

(B) *Water phantom with a full-sized silicone plate downstream of the BP*

The comparison of the TOAs of the γ-waves in geometry (B) between the simulation and experiment is shown in Figure 4 (a-2). The TOA is approximately 3.5 μs longer than that of (A) due to the silicone having a lower sound speed than the surrounding water. As illustrated in Figure 4 (a-2), the discrepancy in TOAs was within 1 μs at all measurement points. The corresponding distance (Figure 4 (b-2)) was <1 mm throughout the region, except when X ≥ 32 mm.

(C) *Water phantom with a half-sized silicone plate downstream of the BP*

The comparison of the TOAs of the γ-waves in geometry (C) between simulation and experiment is shown in Figure 4 (a-3). As expected, the X < 0 region approaches (A) with movement off-axis while the X > 0 region approaches (B). The superposition of the waves diffracted at the silicone edge and those passing through the silicone plate occurs in the region of 0 < X < 15 mm (see the video data in the Supplementary Material). The dip at X = 15 mm indicates

the end of this superposition. The TOA difference is within 1 μs except for the position where the waveform significantly changes near the diffraction edge (X = 0 mm) (Figure 4 (a-3) and Figure 5 (C)), and the corresponding distance is <1 mm except for the region at the diffraction edge and >30 mm away from the beam axis (Figure 4 (b-3)).

(D) *Water phantom with a half-sized bone plate in the beam path*

The TOAs of the γ-waves in geometry (D) between the simulation and experiment are compared in Figure 4 (a-4). Here, the BP is split into two peaks depending on the presence or absence of a bone plate in the beam path, and γ-waves were generated corresponding to each of the split BPs. The minimum of the TOA for the first peak is shifted to X < 0 because the center of the deeper BP is shifted to X < 0. The minimum TOA of the second peak is shifted to X > 0 for the same reason. The two peaks merged at X ~23 mm, and the second peak was not visible further off-axis (see the video data in the Supplementary Material). As shown in Figure 4 (a-4), for the first peak, the TOA difference was within 1 μs at X ≤ 30 mm, and the corresponding distance was <1 mm at X ≤ 27 mm (Figure 4 (b-4)). However, for the second peak, the TOA difference exceeded 1 μs over a wide range of X < 0, and the corresponding distance was >1 mm (but <2 mm) over larger areas (Figure 4 (b-4)).

3.3 Acoustic pressure

The P_{peak} in the experiment and simulation for each geometry is plotted in Figure 6. For the first peak, the pressure distribution in the simulation closely resembled that of the experiment, with discrepancies of 3.0% 0.0%, 2.9%, and 2.3% when comparing the FWHMs for geometries (A)–(D), respectively. The peak pressure of geometry (D) was approximately half that of the other systems, which reflects the beam being split in half.

Conversely, the second peak of geometry (D) exhibited a significant discrepancy between the simulation and experiment owing to the interference of the echoes shown in Figure 3. The second peak is attributed to the shallower BP formed through the bone plate, which is anticipated to exhibit a peak maximum at X > 0, reflecting the shift in the center of the dose deposition. Additionally, the second peak is anticipated to have a reduced pressure compared with the first due to the greater distance to the sensors. Although the simulations yielded the anticipated results, the

experimental data exhibited a markedly different outcome. In particular, the second peak exhibited a maximum pressure exceeding that of the first peak, developing near X = 0.

Finally, the difference between the pressure-voltage conversion coefficient derived from system (A) and (D) was 13%. This indicates that the output of the OHs fluctuates across days, although this was not so pronounced over a few hours.

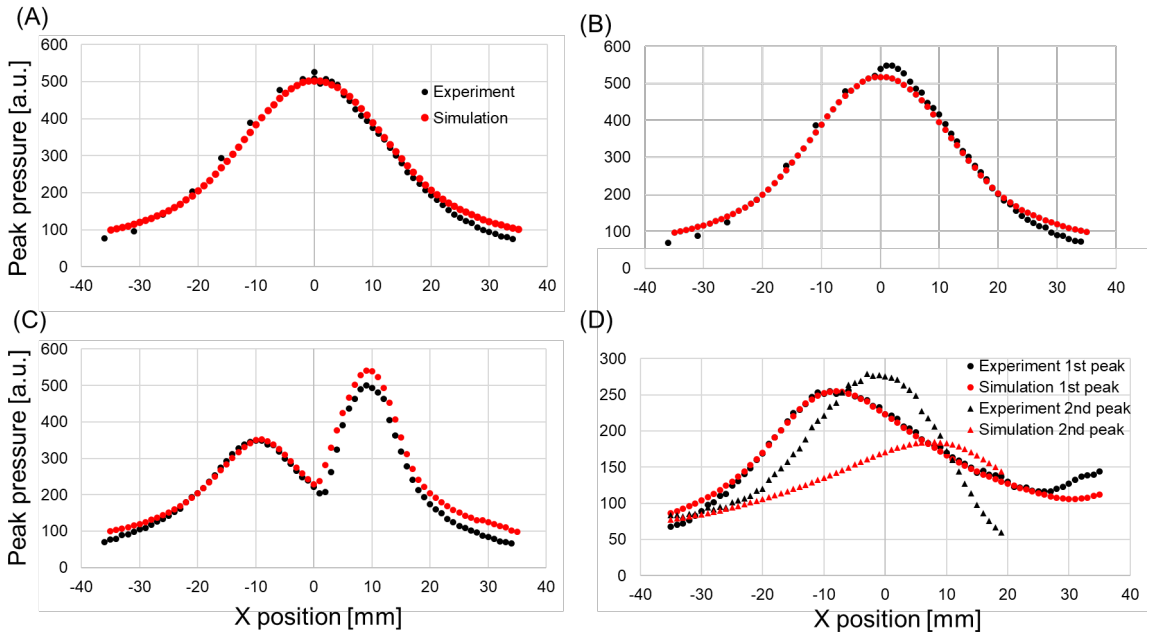


Figure 6. (A)–(D) presents a comparison of simulated (red) and experimental (black) pressure distributions for respective geometries. For (D), the first (circle) and second peak (triangle) are plotted simultaneously. For all experimental data, the standard error of the pressure at each position is also plotted for the first peak, but it is too small to be seen.

4. Discussion

Despite their small size, OHs exhibit a high sensitivity in the low-frequency range of protoacoustic waves, rendering them suitable for proton beam range detection. In this study, we focused on the TOA and compression peak pressure distributions, which are important quantities for localizing the BP and estimating the beam size. We examined whether an OH can describe these quantities in heterogeneous phantoms with sufficient accuracy. Our findings indicate that the measured values are in good agreement with the ground-truth simulations, even without deconvolving the data by the detector's response functions; the only correction that was required was the time shift originating from the delay of the detection system. Moreover, no correction was necessary for the oblique incidence of the pressure waves to reproduce the pressure distributions of the ground truth.

Regarding the directivity of the OH, the detection area being considerably smaller than the scale of the protoacoustic wavelength, the phase mixing in the detection area was considered minimum, but the disturbance in the glass body of the detector (Figure 1) could have had an effect on the angular sensitivity. However, as illustrated in Figure 7, the measurement conducted using a sinusoidal wave of 130-kHz (typical frequency of the γ-wave) resulted in a sensitivity drop of only 6% with 30° rotation of the detector. In the current configurations, the angle between the line connecting the BP and the detector and the beam axis is a maximum of 39°, indicating minimal possible effect on the pressure distributions due to angular dependence.

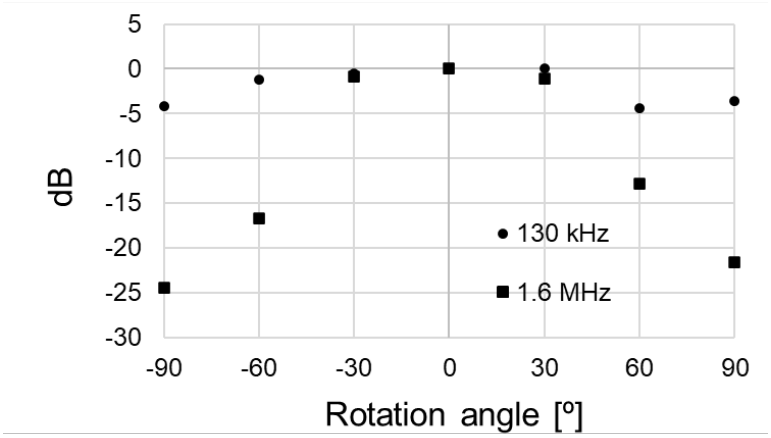


Figure 7. Angular dependence of the optical hydrophone for 130 kHz sinusoidal wave. Data for 1.6 MHz is shown together as a reference. The sinusoidal waves were emitted from the hydrophones V391-SU and V397-SU (Olympus, Waltham, USA) in water tank, respectively, with an input from the arbitrary waveform generator.

As illustrated in Figure 3, the TOA and pressure distributions exhibit satisfactory agreement with the ground truth for the initial compression peak, however, the waveforms following this peak are distorted by the echoes in the detector. The second positive peak in geometry (D), though still discernible, was considerably affected by the echoes. These echoes, however, may be removed by the deconvolutions.[16,17,29] For example, the dashed curves in Figure 3 show the deconvoluted waveforms obtained by applying the transfer function, defined by

$$T(f) = \frac{FT[S(t)]}{FT[p(t)]}$$

to the filtered waveforms. Here $p(t)$ and $S(t)$ are simulated and measured waveforms at X = 0 in geometry (A). The observation that the waveforms in geometry (B)-(D) deconvolved with the same transfer function are less affected by echoes and mostly in agreement with the simulated waveforms is encouraging, although further analysis is necessary to ascertain whether the same transfer function can be applied to more general experimental settings (different sensor positions and beam energies) and is currently under investigation. Despite the good agreement of the first compression peaks, it was observed that the second compression peak of geometry (D) exhibited a greater deviation from the simulation. The shift occurred in the same direction as the first peak during the deconvolution process, with a resulting deviation from the simulated peak of 1.1 μs (1.7 mm in distance). This discrepancy may be partially explained by the slight variation in bone plate thickness across the plate.

One of the challenges associated with protoacoustics is the typically weak generated pressure, which makes the detection of the beam range of all spots in the treatment fields at the clinically relevant dose challenging. As demonstrated in this study, prediction of the pressure magnitude by simulation prior to the treatment can enable identification of the optimum sensor position to ensure a sufficient signal-to-noise ratio and the spots at which the ranges are detectable. In fact, the position experiencing the maximum pressure is not necessarily on the beam axis in the presence of inhomogeneity; in geometries (C) and (D), the maximum sound pressure is obtained at a position 10 mm from the beam axis. It is particularly vital to exercise caution when using the pencil beam of geometry (D), since its pressure is half that of the others and the signal might not be detected if the delivered dose is not large enough.

For increased compatibility of OH with these applications, it is desirable to reduce the daily variation of the output. Regarding the optimum sensor position, the pre-simulations can also help predict the positions where the variation of TOA against detector misalignment can be minimal, thereby facilitating robust range measurements for clinical practice. For instance, the position near the diffraction edge in geometry (D) could cause large variations in TOA with a small misalignment and hence is not optimum for range measurement. After identifying the optimal measurement positions and detectable pencil beams through simulation, the IGRT devices mounted on the beam delivery systems may be employed to accurately position the detectors to the designated location.

Finally, further investigations are needed to overcome some limitations associated with the accelerator and detector. First, this study was performed only with a 100-MeV proton beam from FFA. This is a relatively low-energy beam that produces a steeper BP compared to the beam energies used for deep-seated abdominal tumors. FFA does not use the energy degrader and produces a BP that is even steeper than the beam provided by cyclotron-based clinical systems. In addition, the FFA produces the instantaneous proton pulse (20–30 ns), whereas clinical machines use beams of longer duration (>3 μs). Although there are several studies which successfully detected the protoacoustic waves with a single pulse with clinical machines,[15,30] both higher energy beams and longer-duration pulses result in a broader pressure peak of the protoacoustic wave, which may be more affected by detector echoes. Measurements on the patient surface, particularly with multiple sensors might experience more pronounced effects of diffraction and reflection from the surroundings of the sensors and neighboring sensors[23]. These issues need to be addressed in future studies.

5. Conclusion

In this study, the accuracy of the TOA and compression peak pressures of the protoacoustic waves detected by the OH in heterogeneous geometries were investigated. The measurements were conducted at regions downstream of the BP, where the pressure magnitude is relatively high and the sensitivity of TOA against the range shift is large. The deviation of TOA of the first compression peak against the ground-truth simulation was primarily attributed to the minimal alignment errors (<1 mm) of the measurement devices and phantoms. The compression peak pressure distribution closely resembled the ground truth, with the FWHM differences of 0.0%–3.0% for the tested geometries.

Furthermore, these results were obtained without considerations of the detector size effect and the angle dependence of the sensitivity. Nevertheless, further assessment and development are necessary for future clinical applications regarding the finite pulse length of clinical accelerators and high energy beams for deep-seated tumors.

Acknowledgments

TM thanks Dr. Taisuke Takayanagi and Prof. Nobuki Kudo of Hokkaido University for the precious advice, and Mr. Cristiano Tomasi, and Drs. Morita and Tohyama of Opto Science Inc. for their professional support. This research was supported by JSPS KAKENHI grant number 21H02859 and 21K19434 and 24K22101 and 24K18782 and the JST FOREST Program (grant number JPMJFR200X, Japan).

Conflicts of Interest Statement

Wolfgang Rohringer is paid by XARION Laser Acoustics GmbH, Vienna, Austria. Other authors have no conflicts of interest.

Data availability

Data supporting the findings of this study are available from the corresponding author upon reasonable request.

References

1. Paganetti H, Beltran C, Both S, et al. Roadmap: proton therapy physics and biology. *Physics in Medicine & Biology*. 2021;66(5). doi:10.1088/1361-6560/abcd16.
2. Parodi K, Assmann W. Ionoacoustics: A new direct method for range verification. *Modern Physics Letters A*. 2015;30(17):1540025. doi:10.1142/S0217732315400258.
3. Hickling S, Xiang L, Jones KC, et al. Ionizing radiation-induced acoustics for radiotherapy and diagnostic radiology applications. *Medical Physics*. 2018;45(7):e707-e721. doi:10.1002/mp.12929.
4. Nishio T, Miyatake A, Ogino T, Nakagawa K, Saijo N, Esumi H. The development and clinical use of a beam ON-LINE PET system mounted on a rotating gantry port in proton therapy. *International Journal of Radiation*

Oncology, Biology, Physics. 2010;76(1):277-286. doi:10.1016/j.ijrobp.2009.05.065.

5. Richter C, Pausch G, Barczyk S, et al. First clinical application of a prompt gamma based in vivo proton range verification system. *Radiotherapy & Oncology*. 2016;118(2):232-237. doi:10.1016/j.radonc.2016.01.004.
6. Parodi K, Yamaya T, Moskal P. Experience and new prospects of PET imaging for ion beam therapy monitoring. *Zeitschrift für Medizinische Physik*. 2023;33(1):22-34. doi:10.1016/j.zemedi.2022.11.001.
7. Hayakawa Y, Tada J, Arai N, et al. Acoustic pulse generated in a patient during treatment by pulsed proton radiation beam. *Radiation Oncology Investigations*. 1995;3(1):42-45. doi:10.1002/roi.2970030107.
8. Kim K, Pandey PK, Gonzalez G, Chen Y, Xiang L. Simulation study of protoacoustics as a real-time in-line dosimetry tool for FLASH proton therapy. *Medical Physics*. 2023. doi:10.1002/mp.16894.
9. El Naqa I, Pogue BW, Zhang R, et al. Image guidance for FLASH radiotherapy. *Medical Physics*. 2022;49(6):4109-4122. doi:10.1002/mp.15662.
10. Bjegovic K, Sun L, Pandey P, et al. 4D in vivo dosimetry for a FLASH electron beam using radiation-induced acoustic imaging. *Physics in Medicine & Biology*. 2024;69(11). doi: 10.1088/1361-6560/ad4950.
11. Sueyasu S, Takayanagi T, Miyazaki K, et al. Ionoacoustic application of an optical hydrophone to detect proton beam range in water. *Medical Physics*. 2023;50(4):2438-2449. doi:10.1002/mp.16189.
12. Tada J, Hayakawa Y, Hosono K, et al. Time resolved properties of acoustic pulses generated in water and in soft tissue by pulsed proton beam irradiation--a possibility of doses distribution monitoring in proton radiation therapy. *Medical Physics*. 1991;18(6):1100-4. doi: 10.1118/1.596618.
13. Jones KC, Vander Stappen F, Sehgal CM, Avery S. Acoustic time-of-flight for proton range verification in water. *Medical Physics*. 2016;43(9):5213. doi:10.1118/1.4961120.
14. Lehrack S, Assmann W, Bertrand D, et al. Submillimeter ionoacoustic range determination for protons in water at a clinical synchrocyclotron. *Physics in Medicine & Biology*. 2017;62(17):L20-L30. doi: 10.1088/1361-6560/aa81f8.
15. Patch SK, Nguyen C, Dominguez-Ramirez D, et al. Thermoacoustic range verification during pencil beam delivery of a clinical plan to an abdominal imaging phantom. *Radiotherapy & Oncology*. 2021;159:224-230. doi:10.1016/j.radonc.2021.03.027.

16. Schauer J, Wieser HP, Lascaud J, et al. Range verification of a clinical proton beam in an abdominal phantom by co-registration of ionoacoustics and ultrasound. *Physics in Medicine & Biology*. 2023;68(12):125009. doi:10.1088/1361-6560/acd834.

17. Lascaud J, Dash P, Wieser HP, et al. Investigating the accuracy of co-registered ionoacoustic and ultrasound images in pulsed proton beams. *Physics in Medicine & Biology*. 2021;66(18):185007. doi:10.1088/1361-6560/ac215e.

18. Kellnberger S, Assmann W, Lehrack S, et al. Ionoacoustic tomography of the proton Bragg peak in combination with ultrasound and optoacoustic imaging. *Scientific Reports*. 2016;6:29305. doi:10.1038/srep29305.

19. Preisser S, Rohringer W, Liu M, et al. All-optical highly sensitive akinetic sensor for ultrasound detection and photoacoustic imaging. *Biomedical Optics Express*. 2016;7(10):4171-4186. doi:10.1364/BOE.7.004171.

20. van der Heiden MS, van Neer P, Wieser HP, et al. Ultrasensitive Optoacoustic Sensor for Dosimetry in Proton Therapy-OMUS4PT.

21. Kuriyama Y. Status and development of a proton FFAG accelerator at KURRI for ADSR study. *Proc of 2011 Particle Accelerator Conference*; 2011. p. 2172-2174.

22. Ishi Y. Status report on FFAG accelerator complex at KURRI. *Proc of the 12th Annual Meeting of Particle Accel Soc of Japan*; 2015. p. 368-370.

23. Sueyasu S, Kasamatsu K, Takayanagi T, et al. Technical note: Application of an optical hydrophone to ionoacoustic range detection in a tissue-mimicking agar phantom. *Medical Physics*. 2023. doi:10.1002/mp.16892.

24. https://www.olympus-ims.com/en/ndt-tutorials/thickness-gauge/appendices-velocities/.

25. Nakamura Y, Takayanagi T, Uesaka T, et al. Technical Note: range verification of pulsed proton beams from fixed-field alternating gradient accelerator by means of time-of-flight measurement of ionoacoustic waves. *Medical Physics*. 2021;48(9):5490-5500. doi:10.1002/mp.15060.

26 Alsanea F, Moskvin V, Stantz KM. Feasibility of RACT for 3D dose measurement and range verification in a water phantom. *Medical Physics*. 2015;42(2):937-946. doi:10.1118/1.4906241.

27. Treeby BE, Cox BT. k-Wave: MATLAB toolbox for the simulation and reconstruction of photoacoustic wave

fields. *Journal of Biomedical Optics*. 2010;15(2):021314. doi:10.1117/1.3360308.

28. Takayanagi T, Uesaka T, Nakamura Y, et al. On-line range verification for proton beam therapy using spherical ionoacoustic waves with resonant frequency. *Scientific Reports*. 2020;10(1):20385. doi:10.1038/s41598-020-77422-2.

29. Haffa D, Yang R, Bin J, et al. I-BEAT: ultrasonic method for online measurement of the energy distribution of a single ion bunch. *Scientific Reports*. 2019;9(1):6714. doi:10.1038/s41598-019-42920-5.

30. Caron J, Gonzalez G, Pandey PK, et al. Single pulse protoacoustic range verification using a clinical synchrocyclotron. Phys Med Biol. 2023;68(4):10.1088/1361-6560/acb2ae. doi: 10.1088/1361-6560/acb2ae.